Improved MUSIC-based SMOS RFI Source Detection and Geolocation Algorithm

Hyuk Park, *Member, IEEE*, Verónica González-Gambau, Adriano Camps, *Fellow, IEEE*, Mercé Vall-llossera, *Member, IEEE*

Abstract

The European Space Agency's Soil Moisture and Ocean Salinity (SMOS) mission has been providing L-band brightness temperature using its instrument, the Microwave Imaging Radiometer using Aperture Synthesis (MIRAS). In the measurements, the negative effect of Radio-Frequency Interference (RFI) is clearly present, deteriorating the quality of geophysical parameter retrieval. Detection and geolocation of RFI sources are essential to remove or at least mitigate the RFI impacts, and ultimately improve the performance of parameter retrieval. This paper discusses a new approach to SMOS RFI source detection, based on MUSIC (MUltiple SIgnal Classification) algorithm. Recently, the feasibility of MUSIC DOA (Direction Of Arrival) estimation has been shown for the RFI source detection of the Synthetic Aperture Interferometric Radiometer. This paper refines MUSIC RFI source detection algorithm, and tailors it to the SMOS scenario. To consolidate the RFI source detection procedure, several required steps are devised, including the rank estimation of the covariance matrix, local peak detection and thresholds, and multiple-snapshot processing. The developed method is tested using a number of SMOS visibility samples. In the test results, the MUSIC method shows an improvement on the accuracy and precision of the RFI source geolocation, compared with a simple detection method based on the local peaks of Brightness Temperature (BT) images. The MUSIC results especially outperform the SMOS BT image on the spatial resolution.

Index Terms

Radio-Frequency Interferences (RFI), synthetic aperture radiometry, microwave radiometry, beamforming, Direction of Arrival (DOA) estimation, Soil Moisture and Ocean Salinity (SMOS) mission.

H. Park, A. Camps, and M. Vall-llossera are with the Remote Sensing Laboratory, Department of Signal Theory and Communication, Universitat Politècnica de Catalunya (UPC), 08034 Barcelona, Spain, and also with the Institut d'Estudis Espacials de Catalunya (IEEC) /Universitat Politècnica de Catalunya (UPC), 08034 Barcelona, Spain (e-mail: park.hyuk@tsc.upc.edu, camps@tsc.upc.edu, merce@tsc.upc.edu). V. González-Gambau is with the Department of Physical Oceanography, Institute of Marine Sciece, CSIC, and with the SMOS Barcelona Expert Centre, 08003 Barcelona, Spain (e-mail: vgonzalez@icm.csic.es).

Manuscript received

This work was supported by the Spanish Ministry of Economy and Competitiveness under Grants AYA2011-29183-C02-01/ESP, by ICREA Académia, and through the National R+D Plan by means of MIDAS-7 project AYA2012-39356-C05. The work of H. Park was supported by the Juan de la Cierva programme of the Spanish Ministry of Economy and Competitiveness, and by the National Research Foundation of Korea Grant funded by the Korean Government [NRF-2011-357-D00273].

I. INTRODUCTION

The European Space Agency (ESA) Soil Moisture and Ocean Salinity (SMOS) mission was launched on November 2, 2009. The main objective of SMOS is providing information of soil moisture [1], and sea surface salinity [2] with a spatial resolution of 35-50 km. Since its operational phase, multi-angular polarimetric Brightness Temperature (BT) global maps are routinely generated, from which geophysical parameters are estimated. The SMOS single payload is an L-band radiometer, called "Microwave Imaging Radiometer using Aperture Synthesis (MIRAS)". MIRAS is a spaceborne interferometric radiometer that generates BT snapshots every 1.2 seconds. In order to obtain high spatial resolution, MIRAS employs a Y-shaped antenna array with 69 elements [3].

MIRAS operates in a protected frequency band for radio astronomy and passive remote sensing (1400-1427 MHz). According to the International Telecommunications Union Radiocommunication sector (ITU-R) Radio Regulations, the emission within the band is prohibited [4]. However, Radio-Frequency Interferences (RFI) have been detected since the first in-orbit measurements. RFI hamper the geophysical parameter retrieval in the affected pixels [5]–[8]. The interference nature in the impulse response of MIRAS makes contaminations even more serious [5], [7]. MIRAS has high side lobes and six star-shape tails of the impulse response, and therefore a single strong source often causes a six star-shape tails following the secondary lobes in the SMOS snapshot. They affect much larger areas, often corrupting whole parts of BT snapshot (see Fig. 1). A single RFI source corrupts not only one snapshot, but also it can destroy a large set of snapshots. These RFI sources are located in many regions over the world, i.e., mainly over land, and also affecting the oceans. Many of them have been identified and turned off by the corresponding national authorities [5], [7], [10]. However, there are still many RFI sources that must be identified and switched off.

As a solution to the RFI contamination problem, mitigation techniques have been considered [8]–[12]. Another solution is switching-off all the illegal emitters within the protected band, and enforcing emission regulations. To achieve this, it is important to provide the most accurate geolocation of the RFI sources.

This paper presents an improved method to detect and geolocate RFI sources in SMOS imagery. Recently, a novel algorithm for RFI source localization has been proposed for synthetic aperture interferometric radiometers (SAIR) [13], [14]. The method takes advantage of the Direction Of Arrival (DOA) estimation techniques for the localization of RFI sources in SAIR imagery. In [13], the feasibility of DOA estimation for SAIR RFI localization was demonstrated with promising results of MUSIC (MUltiple SIgnal Classification) algorithm.

In this paper, the MUSIC algorithm for the geolocation of SMOS RFI sources is further elaborated as compared to the previous study in [14]. First, more SMOS visibility samples (4,800 samples) are tested, which are measured along the multiple overpasses over specific regions. Accordingly the multiple-snapshot process are demonstrated, whereas the previous study [14] stayed on a single snapshot-wise discussion. Another improvement is that this paper discusses a rank estimation of the covariance matrix, local peak detection, and thresholding, which are not included in [13], [14]. These make the MUSIC method to be an automatic process. In Section II, existing SMOS RFI source localization methods are briefly discussed showing the limitations of the methods. In Section III, the

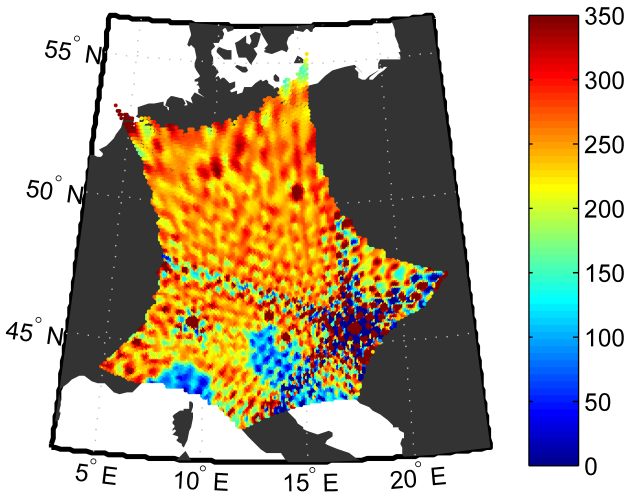

Fig. 1. SMOS snapshot showing a very strong RFI emission. Note the high sidelobe levels of RFI emission contaminating the whole image.

MUSIC algorithm is tailored to SMOS visibility samples. They are followed by a demonstration of the method and performance analysis. Finally, in Section V, we summarize and present the conclusions.

II. SMOS RFI Detection using the BT Images

Before discussing the proposed algorithm, existing SMOS RFI detection methods are briefly reviewed. It is good to start by clarifying the understanding of RFI detection in this paper: geolocation of the RFI emitting sources in SMOS images as in [10], [15], [16]. This objective is somehow different from the RFI detection methods in [17]–[19], which focus on discriminating (flagging) all contaminated measurement pixels rather than locating the RFI source position.

Despite the differences between the SMOS RFI source geolocation algorithms presented in [10], [15], [16], their main procedures are similar: look for local maximum values within a certain threshold on the BT snapshots. These methods are based on the fact that the most RFI sources are point-wise and cause BT values over the natural emission limits (BT $>$ 350 K). After finding the local maxima, the algorithms are refined to improve the false-alarm rate. Because of the synthetic aperture interferometric principles of MIRAS, sidelobes of strong RFI sources exhibit large fluctuation. These sidelobes appear as false alarms, with BT $>$ 350 K (see Fig. 1), and complicate an accurate detection of real RFI sources. To reduce the false alarm rate, RFI source geolocation recorded in the multiple snapshots can be used [10], [15]. Incidence angle filtering is also effective, selecting the RFI sources close to nadir. In [15], a cluster selection was used to cope with false alarms. RFI candidate spots placed within a certain angular distance are grouped as a single cluster, and one maximum point is found by cubic interpolation of those spots. In that way, a single RFI source is determined from many RFI candidate spots, discarding false alarms.

Although these methods have shown adequate performance [7], [10], [15], the accuracy in the RFI source geolocations can deteriorate in some cases. For example, in [15], it was reported that the estimation of the source

location could be biased in the following cases:

1) non-uniform background scenes, e.g., images over coastlines [16];
2) influence of very strong RFI sources;
3) two or more closely spaced RFI.

In extreme cases of 2) and 3), the relatively weak RFI sources cannot even be shown separately, merged as an extended source with the aggregated effect of multiple emitters. Then the geolocations of the individual RFI sources become very difficult.

From the viewpoint of imaging systems, the three cases above are mainly affected by the limitations of the angular resolution and the sidelobe levels. The SMOS imaging can be modeled as liner imaging system, i.e., a convolution of Point Spread Function (PSF) with the input BT image. Therefore, the pixels with the distances shorter than the width of PSF are affected to each other. It means that a strong source affects weak sources closely located, making their peaks are shifted to the direction of strong source, and the finally those RFI source locations detected by the biased peak position.

The SMOS RFI source geolocation can be improved by using the DOA estimation techniques with higher angular resolution and lower sidelobes as compared to the classical Discrete Fourier Transform (DFT) method. In [13], this idea was proved showing promising results of the MUSIC RFI source detection in a snapshot-wise.

III. Application of MUSIC Algorithm to SMOS Visibility Samples

In this Section, MUSIC DOA estimation method is adapted for SMOS observation scenario. Additionally, for RFI source detection, several steps are devised and introduced, e.g., the rank estimation of the covariance matrix, peak detection for MUSIC spectrum, and multiple-snapshot processing.

A. Array Signal Model

In order to apply the MUSIC DOA estimation to the SMOS RFI source geolocation, it is convenient to model the SMOS observations as a conventional sensor array. A signal received by a sensor array can be expressed in a compact form as

$$\begin{aligned}\mathbf{y} &= [y_1, y_2, ..., y_N]^T \\ &= \sum_{i=1}^{M} \mathbf{a}(\xi_i, \eta_i) s(\xi_i, \eta_i) + \mathbf{n} \\ &= [\mathbf{a}_1, ..., \mathbf{a}_M]\, \mathbf{s} + \mathbf{n} = \mathbf{A}\mathbf{s} + \mathbf{n}\end{aligned} \tag{1}$$

where $\mathbf{y}$ is the vector of receiver outputs, $\mathbf{s} = [s(\xi_1, \eta_1), ..., s(\xi_M, \eta_M)]^T$ denotes the vector of impinging signals from the (ξ, η) direction, $(\xi, \eta) = (\sin\theta\cos\phi, \sin\theta\sin\phi))$ denotes the direction cosines with respect to the X and Y axes, $\mathbf{n} = [n_1, n_2, ..., n_N]^T$ is the receiver noise vector, $\mathbf{a}(\xi_i, \eta_i)$ is the steering vector of the signal coming from (ξ_i, η_i), and $\mathbf{A}$ is the steering matrix formed by piling up the different steering vectors. The size of the steering

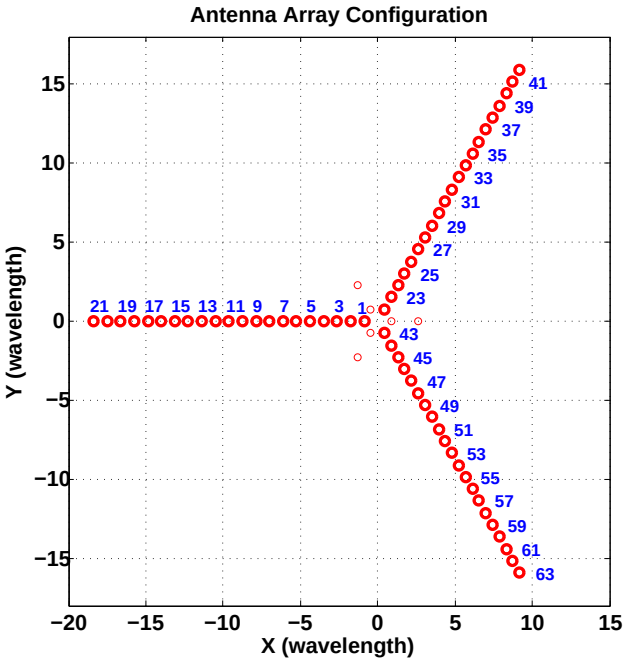

Fig. 2. SMOS Y-shaped array configuration. The antenna elements are indexed with number. Redundant antennas are not considered.

matrix is equal to the number of antenna elements (N rows) times the number of signal sources (M columns). The steering vector for the mth signal is given by

$$\mathbf{a}_m(\xi_m, \eta_m) = \left[e^{-\ j\frac{2\pi}{\lambda}(X_1\xi_m + \ Y_1\eta_m)}, ..., e^{-\ j\frac{2\pi}{\lambda}(X_n\xi_m + \ Y_n\eta_m)} ..., e^{-\ j\frac{2\pi}{\lambda}(X_N\xi_m + \ Y_N\eta_m)}\right]^T \tag{2}$$

where (X_n, Y_n) denotes the nth antenna position, and λ is the wavelength. MIRAS has Y-shaped array with 69 antenna elements spaced by 0.875λ, shown in Fig. 2. According to the antenna index, the steering vector can be constructed. For example, the antenna position of 23rd element is $(X_{23}, Y_{23}) = (2{\cdot}0.875\lambda\cos 60°, 2{\cdot}0.875\lambda\sin 60°)$, and the 23rd element of steering vector can be obtained as in (2).

B. Covariance Matrix Construction

To calculate the MUSIC spatial spectra, the covariance matrix is first obtained. In [13], [21], it is shown that visibility samples of SMOS are equivalent to the elements of the covariance matrix. Actually, both are obtained by cross-correlating the outputs of each antenna pair:

$$\mathbf{R} = \left\langle \mathbf{y}\mathbf{y}^H \right\rangle \tag{3}$$

where the superscript ^{H} denotes the Hermitian transpose. Hence, the covariance matrix can be directly constructed from the calibrated visibility samples (SMOS L1A data). For example, the element of covariance matrix at 21st

row and 48th column is

$$R_{21,48} = \left\langle y_{21} y_{48}^H \right\rangle \tag{4}$$

$$= V_{21,48} \tag{5}$$

where $V_{21,48}$ denotes the visibility samples by correlating the 21st and 48th antenna outputs.

C. Eigenvalue Decomposition of the Covariance Matrix

The MUSIC method starts dividing the covariance matrix into the signal and noise subspaces [22], [23]. The eigenvalue decomposition of the covariance matrix is

$$\mathbf{R} = \sum_{k=1}^{N} \lambda_k \mathbf{u}_k \mathbf{u}_k^H \tag{6}$$

where λ_k and u_k are the kth eigenvalue and its corresponding eigenvector, respectively. If the number of signal sources is given by M_s, the eigenvalues in the ideal observation are

$$\lambda_1 \geq ... \geq \lambda_{M_s} > \lambda_{M_s+1} = ... = \lambda_N = \sigma_n^2 \tag{7}$$

where σ_n^2 is the noise power. It means that the covariance matrix can be decomposed into M_s eigenvalues and eigenvectors (composing signal subspace), and $N - M_s$ eigenvalues and eigenvectors (composing noise subspace), i.e.,

$$\mathbf{R} = \begin{bmatrix} \mathbf{U_s} & \mathbf{U_n} \end{bmatrix} \begin{bmatrix} \mathbf{\Lambda_s} & \mathbf{0} \\ \mathbf{0} & \sigma_n^2 \mathbf{I} \end{bmatrix} \begin{bmatrix} \mathbf{U_s} & \mathbf{U_n} \end{bmatrix}^H. \tag{8}$$

The covariance matrix splits into two sets, generating independent linear spaces: the signal subspace $\mathbf{U_s}$, and the noise subspace $\mathbf{U_n}$.

MUSIC algorithm is based on the fact that noise eigenvectors are orthogonal to the signal steering vectors. The spatial pseudo-spectrum (unitless) of MUSIC is given by

$$P_M(\xi, \eta) = \frac{1}{\mathbf{a}^H(\xi, \eta) \mathbf{U_n} \mathbf{U_n}^H \mathbf{a}(\xi, \eta)}. \tag{9}$$

The MUSIC estimator $P_M(\xi, \eta)$ is a measure of the orthogonality between the steering vector $\mathbf{a}(\xi, \eta)$ and the noise subspace $\mathbf{U_n}$, and therefore it produces peaks in the directions of the signal sources.

The MUSIC DOA estimation is a super-resolution method that outperforms the DFT method [22], [23]. On the other hand, the MUSIC algorithm requires exact determination of the effective rank of the covariance matrix, i.e., the number of signal sources, M_s in (7). Incorrect source number estimation would cause deterioration of the DOA estimation performance, especially in the case of low signal-to-noise ratio (SNR).The impact of rank estimation on MUSIC spectra is illustrated in Appendix. In some applications, the number of signals can be estimated a priori. In SMOS observations, however, the number of RFI sources is unknown, and it has to be inferred for each snapshot.

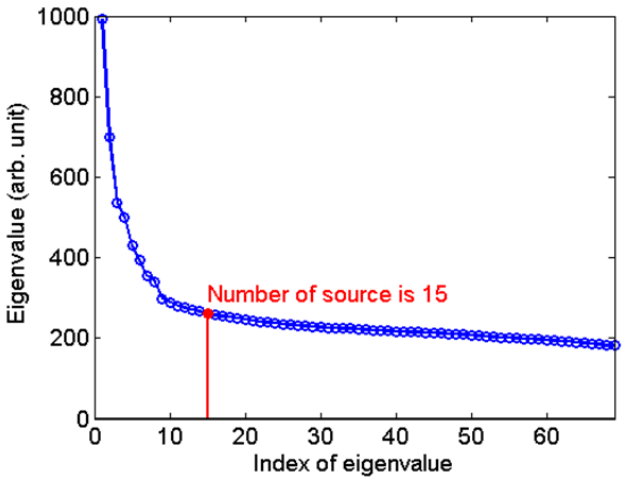

Fig. 3. Eigenvalues of SMOS covariance matrix, sorted in descending order. The elbow of the eigenvalue plot indicates the number of sources for the MUSIC algorithm.

D. Rank Estimation of the Covariance Matrix

For MUSIC DOA estimation, the Akaike Information Criterion (AIC) and the Minimum Description Length (MDL) algorithms are frequently used to estimate the number of sources [24], [25]. However, it is reported that both methods incorrectly estimate under low SNR and small number of samples [26]. The SMOS observation is in the condition of the low SNR and the small number of samples compare to other sensor array system. If K snapshots are used to estimate the covariance matrix, the AIC and MDL for the MUSIC Algorithm are defined by

$$AIC(M_s) = -K(N-1)\log\left\{\frac{\left[\prod_{n=M_s+1}^{N}\lambda_n\right]^{1/(N-M_s)}}{\frac{1}{N-M_s}\sum_{n=M_s+1}^{N}\lambda_n}\right\} + M_s(2N-M_s), \tag{10}$$

$$MDL(M_s) = -K(N-1)\log\left\{\frac{\left[\prod_{n=M_s+1}^{N}\lambda_n\right]^{1/(N-M_s)}}{\frac{1}{N-M_s}\sum_{n=M_s+1}^{N}\lambda_n}\right\} + \frac{1}{2}M_s(2N-M_s)\log K. \tag{11}$$

The rank M_s is estimated by the point at which the AIC (or MDL) achieves the minimum. The difficulty of applying AIC / MDL to SMOS covariance matrix consists in the number of snapshots K. The SMOS produces a single snapshot on the static assumption, i.e., $K = 1$. Instead of short integrated many snapshots, SMOS produce a single relatively long integrated (1.2 s) snapshot. In this case ($K = 1$), neither AIC nor MDL works properly. We tried to test if any proper constant K for SMOS exists, but the value of K varies a lot according to the visibility matrix. Therefore, it is difficult to directly use the AIC or MDL to estimate the number of SMOS RFI sources. In this study, a new method has been devised.

The rank estimation methods using AIC and MDL are based on the fact that the noise eigenvalues are identical in the ideal case, as shown in (7). This means that the eigenvalue clustering into two parts provides the estimate of

the number of RFI sources. Fig. 3 shows an example of the eigenvalues of SMOS covariance matrix. In the ideal case, the $N - M_s$ smallest eigenvalues are the same, but they are not in practice.

Through the examination of the eigenvalues of SMOS covariance matrix it is found that there is a boundary between the signal and the noise eigenvalues in the slope: 1) in the signal regime the slope of the eigenvalue curve ($\Delta\lambda_k = \lambda_{k+1} - \lambda_k$) varies, 2) in the noise regime the slope of eigenvalues becomes approximately constant (but not zero). Using these characteristics, the eigenvalues can be divided into two regimes, i.e., the variance of the slope can be used to divide the noise and signal space by determining so-called elbow point of eigenvalue plot (see Fig. 3).

It has been empirically found that the variance of five consecutive slopes $C_r(k) = \mathrm{var}\{\Delta\lambda_k, ..., \Delta\lambda_{k+4}\}$ can be effectively used. Then, the rank of the covariance matrix is obtained from the minimum k satisfying $C_r(k) < \kappa_r$, where κ_r is a threshold to limit the variance of the slope. The κ_r is a tuning parameter to appropriately estimate the rank. In the tests with SMOS data, $\kappa_r = 1$ has been found to provide a good split between the signal and noise subspaces (so-called the elbow of curve, see Fig. 3). More examples of eigenvalue plots are presented in Section IV.

E. Calculation of the MUSIC Spectrum

Once the number of sources is estimated by the eigenvalue decomposition of the covariance matrix, the noise subspace can be obtained. Then the MUSIC pseudo-spectrum $P_M(\xi, \eta)$ can be calculated using the steering vector $\mathbf{a}(\xi, \eta)$, and the noise subspace $\mathbf{U_n}$ as (9). In this procedure, the range of (ξ, η) for the MUSIC method is selected as the fundamental hexagon of the SMOS imaging [27]. It is surely possible to calculate the MUSIC spectrum within a smaller area than the fundamental hexagon, e.g., within a Extended Alias Free Field of View (EAF-FOV), or close to nadir direction.

The resolution of the (ξ, η) grid is selected as $(\Delta\xi, \Delta\eta) = (0.001, 0.001)$, which corresponds to less than 0.6 km within the EAF-FOV. The determination of the $(\Delta\xi, \Delta\eta)$ is a tuning parameter which is trade-off between computation time and grid fineness. In the test results using SMOS data (to be seen in Section IV), the accuracy error, the standard deviation, and the spatial resolution are not smaller than about 1 km. It means that the grid resolution of 0.6 km is quite satisfactory for performance evaluation. Actually, when the grid resolution of $(\Delta\xi, \Delta\eta) = (0.0002, 0.0002)$ is used, the accuracy and the standard deviation are different by about 0.001 km compared to the the results of $(\Delta\xi, \Delta\eta) = (0.001, 0.001)$, but the computation time is 40 times longer.

Fig. 4(a) and (c) show, respectively, the SMOS BT and the MUSIC spectrum corresponding to the eigenvalues in Fig. 3. The SMOS BT image is interpolated to the grid resolution of $(\Delta\xi, \Delta\eta) = (0.001, 0.001)$ to match that of MUSIC spectrum. Compared to the SMOS BT, the MUSIC spectrum presents sharper local peaks, which are the RFI sources candidates. The sharper peaks of MUSIC spectrum are clearly shown in the 3-D view (Fig. 4(b) and (d)). Additionally, the sidelobes of the strong peaks are lower in the MUSIC spectrum than in the SMOS BT image. These sharper peaks and the lower sidelobes of the MUSIC spectrum present advantages over the SMOS BT image, for the RFI source detection, which is illustrated in Section IV.

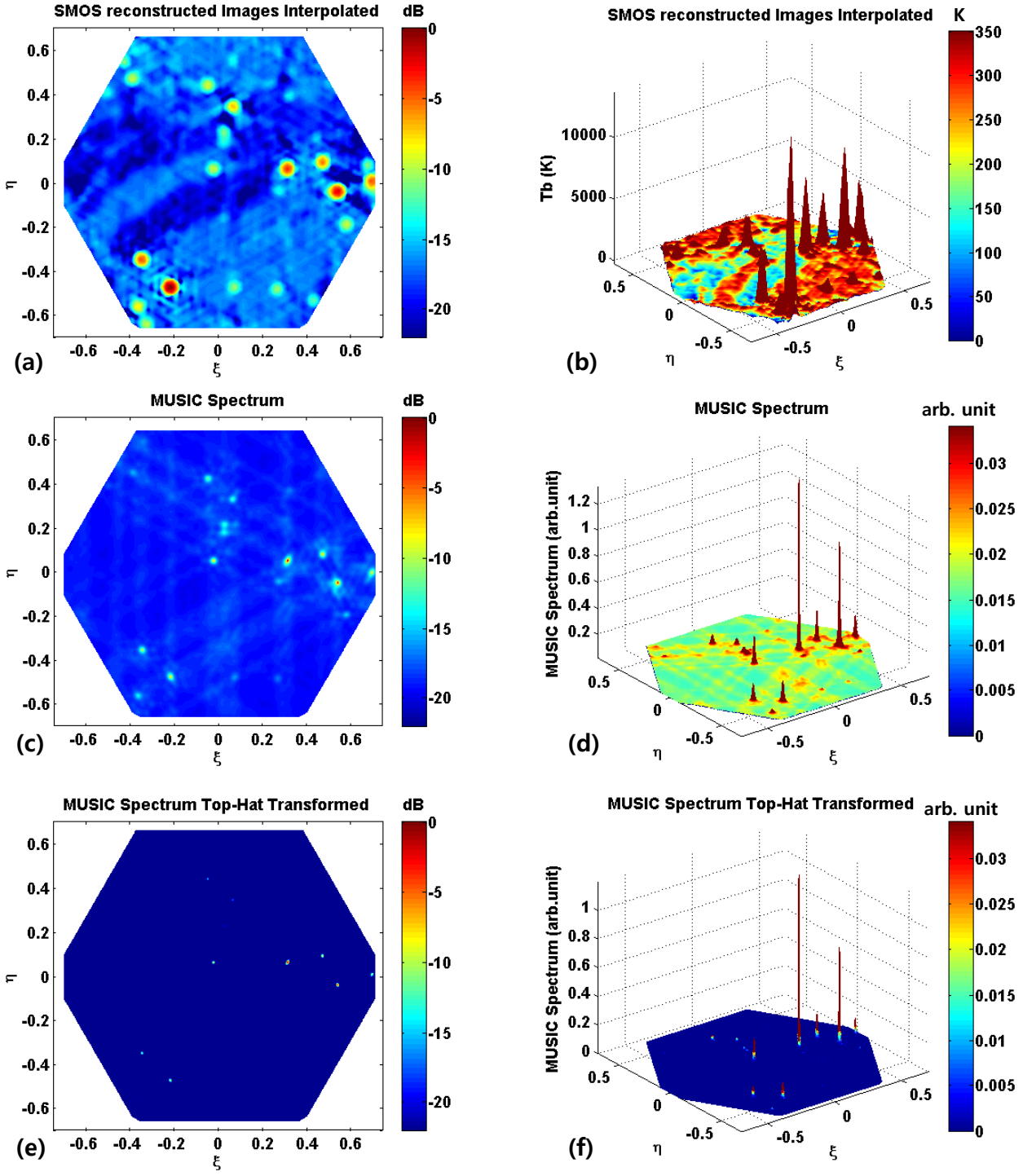

Fig. 4. The first row (a, b) shows SMOS BT images; the second row (c, d) shows MUSIC spectrum estimated from the same visibility samples; and the third row (e, f) shows MUSIC spectrum after top-hat transform. For the purpose of highly visible contrast, the fist column (a, c, e) shows the normalized and log-scaled values, i.e., spectra in dB. The second column (b, d, f) shows 3D-view of spectra in linear scale.

F. Local Peak Detection

After the MUSIC pseudo-spectrum is calculated, the RFI positions in the (ξ, η) domain are determined by the local maxima. For the previous SMOS RFI detection methods using L1C data [8], [10], [15], the local maxima with BT $>$ 350 K are selected as candidates of RFI spots. In the MUSIC pseudo-spectrum, local maxima are selected regardless of the spectrum values, i.e., a fixed threshold cannot be applied. Therefore, a designated peak detection method should be devised.

In this study, a top-hat transform is used to detect the local peaks. The top-hat transform is normally used in morphological image processing for the extraction of small elements and details in the images. It is defined as the difference between the input image and its opening by some structuring element [28]:

$$P_{M,hat}(\xi, \eta) = P_M(\xi, \eta) - P_M(\xi, \eta) \circ b \tag{12}$$

where b is a structuring element, and symbol $\circ$ denotes the opening operation. If a disk-shaped structuring element is used, the opening of an image is equivalent to a low-pass filter. Then top-hat transform as the opening residue is equivalent to a high-pass filtered result [29]. In order to properly extract the peaks, the structuring element b should be well defined. This size of b works similarly to the cut-off spatial frequency of low-pass filtering, which is dependent on the peak width on the MUSIC spectrum. In this study, it has been empirically found that the structuring elements with circular shape, and a radius ranging from 6 to 10 pixels produces an acceptable performance for peak detection. It means that in (ξ, η) domain, the range of (0.001×6) to (0.001×10) is a proper radius for the structuring element of top-hat transform of the SMOS MUSIC spectrum.

Fig. 4(e) and (f) show the top-hat transformed image of MUSIC spectrum. As compared to the MUSIC spectrum in Fig. 4 (d), the top-hat transform preserves the sharp peaks and eliminates other features, such as the poor contrast features.

After the top-hat transformation, an adaptive threshold is employed to convert the MUSIC spectrum to a binary image:

$$P_{M,th} = \begin{cases} 1, & \text{if } P_{M,hat} \geq \kappa_{r,hat} \\ 0, & \text{Otherwise.} \end{cases} \tag{13}$$

In this study, the threshold $\kappa_{r,hat}$ is defined as:

$$\kappa_{r,hat} = mean\{P_{M,hat}\} + C_{hat} \cdot std\{P_{M,hat}\} \tag{14}$$

where C_{hat} is the tuning parameter for thresholding. If high C_{hat} is used, the threshold $\kappa_{r,hat}$ becomes high. Then only high and sharp peaks are remained while the low peaks are discarded. It means that the RFI sources with strong MUSIC spectra are selected, whereas the weak ones are not. In this case, RFI source detection is conservative, i.e., low detection and false alarm rates. For the low C_{hat}, it works the other round, i.e., high detection and false alarm rates. Therefore, C_{hat} should be adjusted and tuned to show the appropriate performance. In this study, $C_{hat} = 1$ is used showing acceptable results by visual inspection.

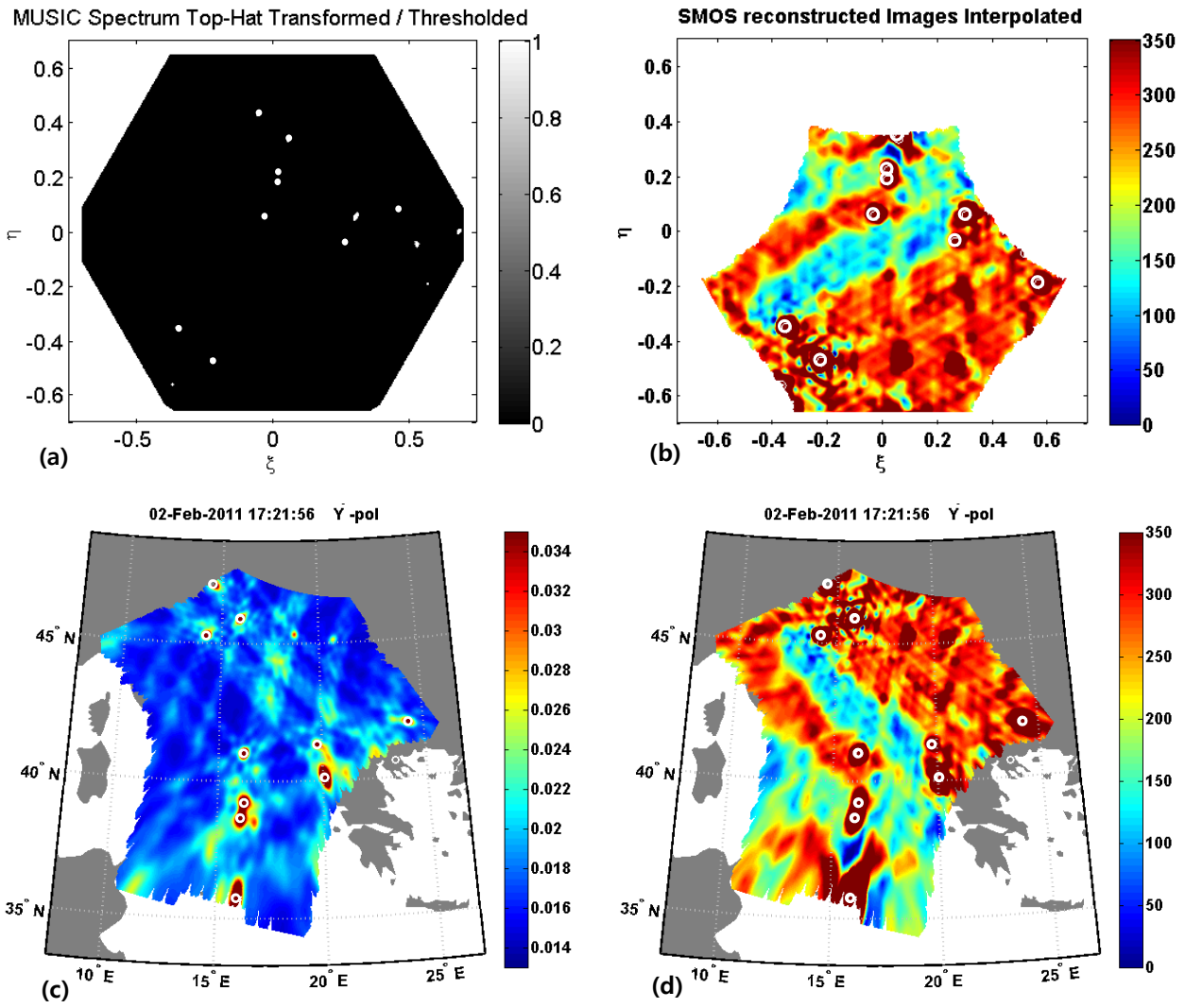

Fig. 5. (a) Detected location of RFI sources after thresholding the top-hat transformed MUSIC spectrum in the antenna reference frame (fundamental hexagon), (b) detected RFI sources superimposed on the SMOS BT, within EAF-FOV in the antenna reference frame. The geo-referenced RFI sources are superimposed on (c) the MUSIC spectrum, and (d) the SMOS BT. White circles depict the RFI source locations detected by MUSIC method.

After thresholding the MUSIC spectrum is transformed into a binary image where the regions around the peaks (RFI spots) are set to 1 and the others to 0. Fig. 5(a) shows the binary image. In each RFI spot the (ξ, η) of the maximum P_M is assigned as the RFI source direction, and only EAF-FOV are selected for the RFI source search, as shown in Fig. 5(b). Finally the RFI source directions are geo-referenced using the information of the SMOS satellite position and attitude, as shown Fig.5(c) and (d). At this stage, RFI sources are detected and geolocated in a single snapshot.

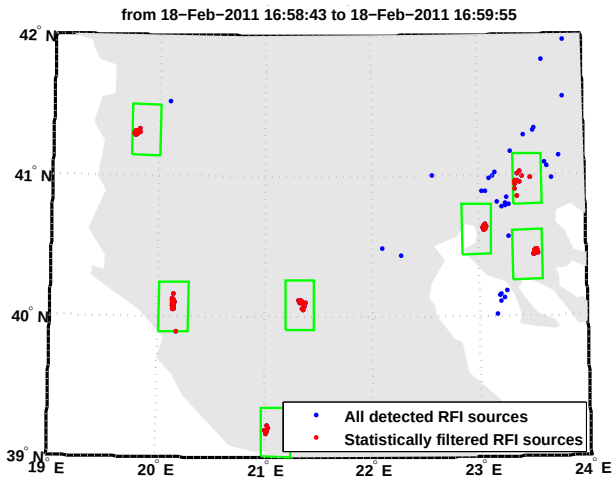

Fig. 6. An example of multiple-snapshot processing. The blue dots and the red dots denote all the RFI spots and the selected ones, respectively. The selected bins are depicted by the green boxes. The bin size of 20 by 20 km and the hit rate of 30% are used.

G. Multiple-Snapshot Processing

RFI sources detected in single snapshot can be post-processed and averaged using multiple snapshots to improve the detection performance, e.g., accuracy of geolocation, and false alarm rate. In this study, a statistical selection technique is considered. First, a certain region is assigned for RFI source search. The region is divided into equal-area bins, and the number of RFI source hits from the multiple snapshots are counted, namely, generating a histogram for geographic points. This approach basically assumes that the RFI sources are not pulsed and isotropic. For the spatial histogram, the bin size should be tuned to satisfy that 1) one bin does not contain more than one RFI source, 2) one RFI source is not contained in different bins. In this study, a bin size of 20 by 20 km is considered, which assumes the detection within the bin as belonging in to the same source [15]. This bin size produces a reasonable separation of RFI sources as shown in Fig. 6.

The analysis of the histogram can be performed using several methods: 1) to assign a given threshold and select only the bins with number of hits above that value or 2) to define a hit rate. Note that the thresholds of the number of hit or hit rate are tunning parameters. If the threshold is too high, for example 80%, the output is a conservative estimate where the RFI sources with weak power are discarded. On the other hand, a low threshold might causes an increase of false alarm rate. The results in Fig. 6 are obtained with a 30% hit rate. In this study, 30% hit rate selects well the RFI sources while discarding the false alarms.

After selecting the bin of RFI sources, the final RFI source geolocation is estimated by averaging points inside the bin. Fig. 6 shows an example of multi-shot processing using 31 snapshots. From all the spots of RFI sources (denoted by blue dots), the concentrated ones (denoted by red dots) in the histogram bins (denoted by green boxes) are selected as the points to be averaged.

IV. Demonstration of MUSIC RFI Source Detection

In Section III, the SMOS RFI source detection procedure using MUSIC algorithm has been discussed. In this Section, the MUSIC RFI detection method is demonstrated with the performance analysis. For this evaluation, we have chosen the test region covering Italy and Greece, which ranges roughly from 5° to 30° in longitude, and from 35° to 48° in latitude. In this region, there are three identified RFI sources used for the accuracy test, named as IT 4, IT 5, and IT 14 in [15]. The geolocations of the three RFI sources are approximately shown in Fig. 7 and 8. An advantage of using this region as a test site is that there are several RFI sources closely located to each other, shown in Fig. 9. These are used for demonstration of RFI geolocation resolution.

In this study, a total of 4,800 SMOS visibility samples has been used, which have been acquired from 2011-02-02 to 2011-03-31. For each day, one or two overpasses across the assigned region are selected (60 overpasses in total), where 80 snapshots are provided in each pass.

Examples of the SMOS BT images and the MUSIC spectra are shown in Fig. 7. The true locations of RFI sources IT 5, 14 and 4 are, respectively, shown and zoomed in the first, second, and the third rows of Fig. 7. The last column, Fig. 7(c), (f), and (i) presents the results of rank estimation of the covariance matrix. They depict well the elbow point of eigenvalues, which separate the signal and the noise subspaces as discussed in section III-D. The correct selection of the noise subspace leads to an acceptable MUSIC spectrum revealing the sharp peaks at the high-power signal sources - RFI sources in this case. Compared to the SMOS BT images, the MUSIC spectrum presents sharper peaks where a strong BT exists.

A. Accuracy and precision of RFI geolocation

Fig. 8 shows the RFI source detection results through the multiple-snapshot processing for true RFI sources. The RFI spots detected from the SMOS BT and the corresponding mean are marked by red dots. The MUSIC ones are marked by blue diamonds, and the geolocations of the true RFI sources are marked by black asterisks. The vicinity of true RFI, denoted by box, is zoomed in the right-bottom corner for convenience. As shown in the figure, the MUSIC results show more concentrated RFI spots and closer to the true RFI, when compared to the SMOS BT results. The distances between the estimated and the true RFI sources are considered as the estimated errors, and listed in Table I. For these three tests, MUSIC errors are about 76% of BT ones. The corresponding standard deviation of the errors are also shown in Table I. The MUSIC ones are about 27% of the BT ones. In all the results of this study, the standard deviation estimated using the MUSIC results are less than 3 km.

As shown in [12, Fig. 5] and mentioned in section II, the estimated source location could be biased (located further inland) around coastlines. Fig. 8(a) also shows the bias. The RFI source IT 5 is located close to coast, about 17 km from the sea. The direction of land is east (righthand side), and therefore the means of estimated RFI source locations are biased to the right-hand side. As compared with the source location estimate from SMOS BT, the MUSIC one shows small bias in Fig. 8(a) thanks to the high spatial resolution.

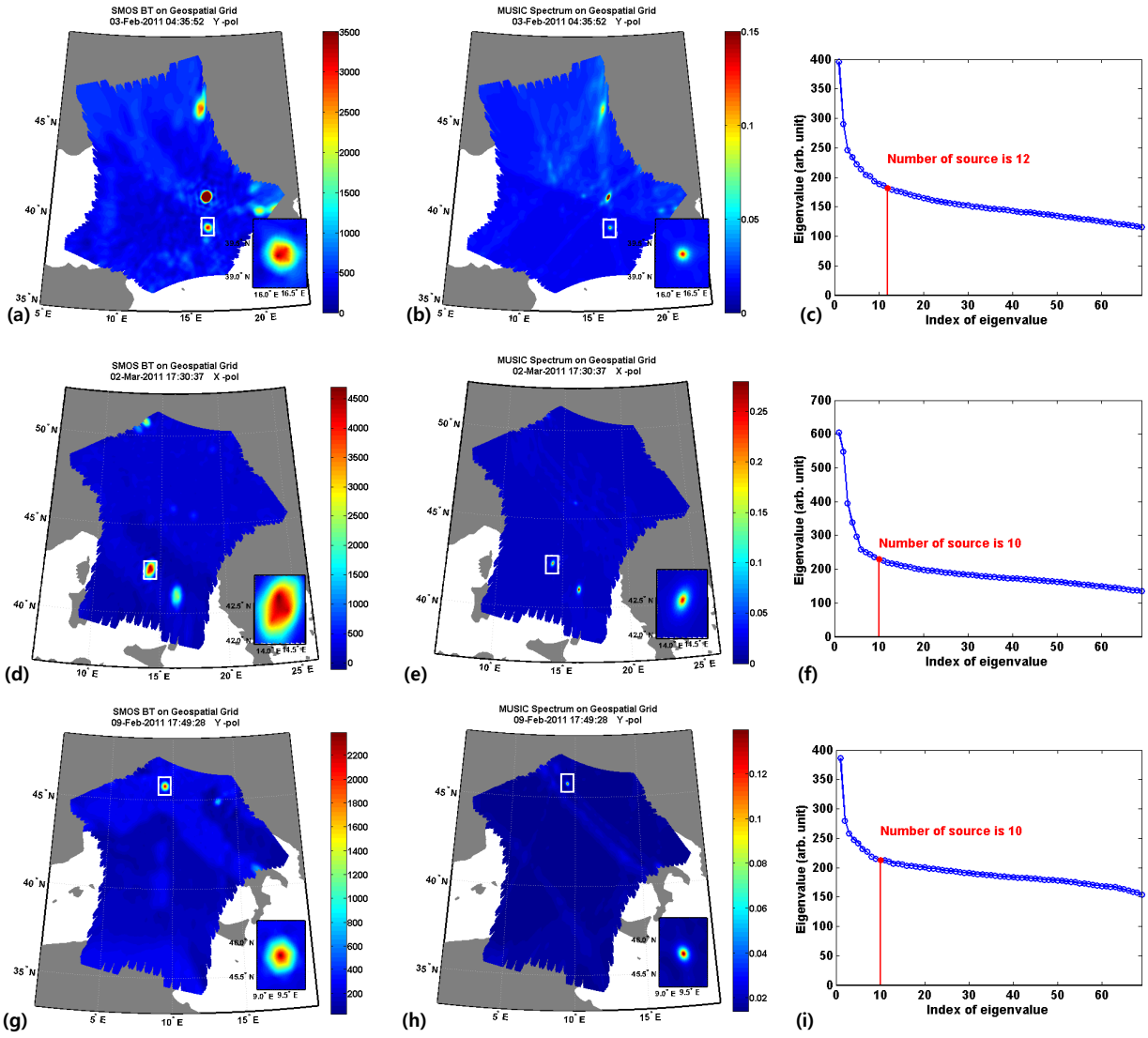

Fig. 7. Comparison of the RFI source detection methods based on the BT images (a, d, g) and the MUSIC spectra (b, e, h). The number of sources is estimated from the elbow point of the eigenvalues of the covariance matrix (c, f, i). The first row (a, b, c), the second row (d, e, f) and the third row (g, h, i) show, respectively, the snapshots covering the RFI sources IT 5, IT 14, and IT 4.

B. Spatial Resolution of RFI geolocation

The resolution of RFI geolocation can be considered as the smallest distance between two detectable RFI sources. From the viewpoint of imaging system, it can be considered as the half power width of the impulse response or the point spread function. In SMOS case, the best spatial resolution is 35 km. Therefore, the best spatial resolution of RFI source geolocation is also 35 km in ideal case, when two identical sources are present over the homogeneous background. In practice, two RFI sources at a distance of about 45 km are still merged together appearing as a single wide spot, as shown in Fig. 9(a), (c), and (e). The distance between the two sources is about 43 km in Fig.

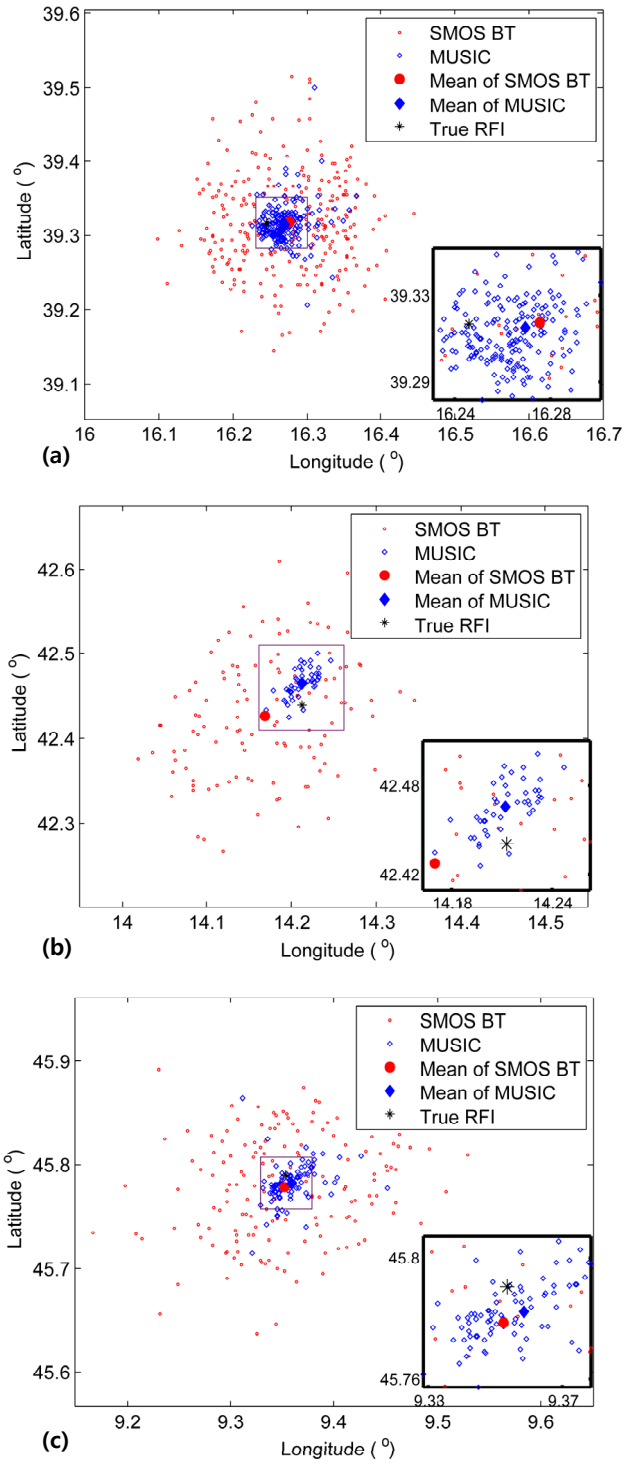

Fig. 8. RFI source detection results of multiple-snapshot processing using 3 different overpasses: (a) IT 5, (b) IT 14, and (c) IT 4.

TABLE I
ACCURACY AND PRECISION TEST RESULTS

		Error (km)	STD (km)
IT 5	BT	2.58	8.50
	MUSIC	2.05	2.62
IT 14	BT	3.79	8.93
	MUSIC	2.79	2.06
IT 4	BT	1.33	6.87
	MUSIC	0.98	1.98

9(a) and (b). In the SMOS BT image, the strong source masks the weak one, making a single elongated RFI spot. However, in the MUSIC spectrum, these are clearly resolved.

In Fig. 9 (d), the MUSIC spectrum also separates two sources at a distance of about 45 km. On the contrary, they appear to be a single elongated source in the SMOS BT image, as seen in Fig. 9(c). This resolution comparison is also apparent in Fig. 9(e) and (f). The left zoom boxes correspond to the same region in Fig. 9(c) and (d), and the superior resolution of MUSIC is well represented. This high spatial resolution is also shown in multi-shot processing. In Fig. 6, those two RFI sources within a small distance are clearly clustered and selected. It means that the MUSIC method stably resolves them over overpasses.

The zoom boxes at the bottom-right of Fig. 9(e) and (f) show the RFI sources with further distances; the distance between the center and the upper ones is about 70 km. In this case, the SMOS BT also shows the separate peaks because the distance of 70 km corresponds to twice the SMOS spatial resolution. In the MUSIC spectrum, these RFI sources are shown as much sharper peaks.

In the test results, the MUSIC method shows better performance of RFI source geolocation than the classical DFT, in terms of the accuracy and the spatial resolution. These results are directly based on that the MUSIC DOA estimation has a higher spatial resolution than the classical DFT method. Although the low SNR of SMOS is not a best condition for MUSIC method, the proposed MUSIC RFI source geolocation are promising, showing high spatial resolution

V. CONCLUSION

In this work, MUSIC DOA estimation technique has been applied to SMOS RFI geolocation. The visibility samples of MIRAS are interpreted as the elements of the covariance matrix of a sensor array, and then high performance MUSIC DOA estimation technique can be applied for RFI source detection. The feasibility of this technique was shown in [13], and in this paper a MUSIC algorithm has been tailored to SMOS measurements, including the rank estimation of the covariance matrix, local peak detection, and multiple-snapshot processing. In each step, the appropriate selection of tunable parameters is provided.

The devised methods have been demonstrated using 4,800 snapshots of measured SMOS visibility samples. In the test results, MUSIC shows the improved performances in terms of accuracy and precision, compared with

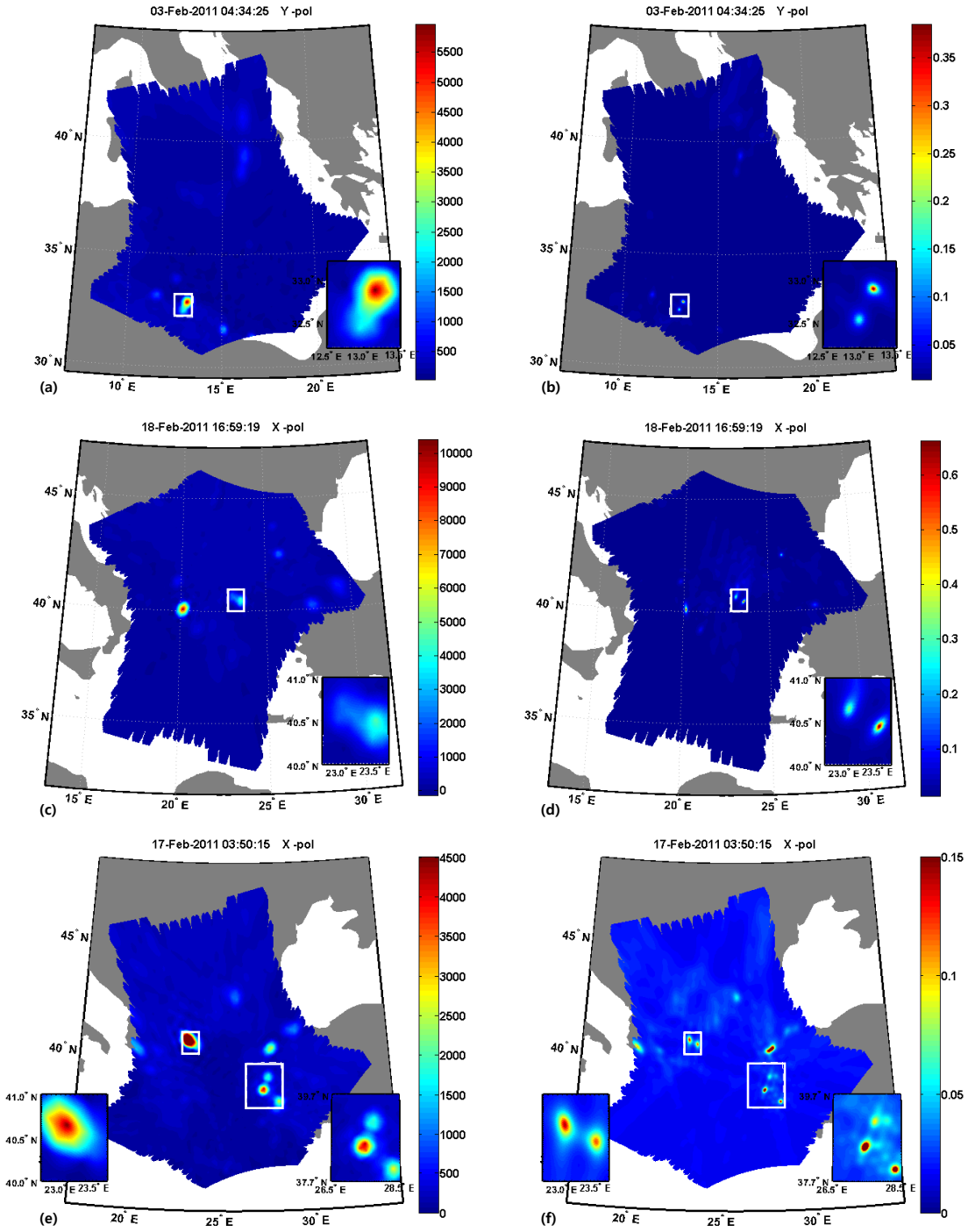

Fig. 9. Comparisons of the resolution of RFI source geolocation. The first column (a, c, e) shows the SMOS BT snapshots, and the second column (b, d, f) shows the MUSIC spectrum.

the SMOS BT. Especially, MUSIC shows its capability to resolve the RFI sources close to each other, which the previous methods could not. In conclusion, the SMOS RFI sources are detected and geolocated accurately and precisely, with high spatial resolution using the devised MUSIC RFI source detection method.

APPENDIX

IMPACT OF RANK ESTIMATION OF COVARIANCE MATRIX ON SMOS MUSIC RFI SOURCE GEOLOCATION

In sensor array studies it has been reported that MUSIC DOA estimation shows improved performance compared to simply finding the peaks of DFT spectra. However, MUSIC requires the a priori information of the number of source, i.e., the rank of the covariance matrix. The wrong estimation of the number of source affects the MUSIC spectra, and finally degrades the performance of DOA estimation. This appendix shows the impact of rank estimation on the SMOS MUSIC RFI source geolocation by comparing the MUSIC spectra obtained from different ranks. Fig. 10(a) shows the SMOS DFT snapshot on (ξ, η) domain, showing the RFI contaminated region (BT>350 K). Fig. 10(b) shows the eigenvalue plot of the visibility covariance matrix. In order to compare the MUSIC spectra, four values of ranks are assumed; M_s = 5, 15, 23 and 35. The rank estimation algorithm described in section III-D estimates the rank of 15, and the elbow point in the eigenvalue plot Fig. 10(b) is also located around M_s = 15. Fig. 10(c) is the MUSIC spectra with M_s = 5. In this case the number of sources is underestimated, and therefore only 5 peaks are presented on MUSIC spectrum. The MUSIC spectrum with M_s = 15 is shown in Fig. (d), which shows more peaks than the case of M_s = 5. Fig. (e) shows the result of M_s = 23. It is the results of somehow overestimation of rank (see the eigenvalue plot in Fig. 10(b)), and therefore it shows more peaks than previous cases. While it shows more peaks, Fig. 10(e) shows more small blobs which cause false alarm. Fig. 10(f) shows the results of quite overestimate rank (M_s = 35). In this case, many small features appear which increase false alarms. Even the shape of peaks deteriorate, which finally degrade the performance of RFI source geolocation.

The method of rank estimation in section III-D has tuning parameter of κ_r. If κ_r is large, the rank estimation is more conservative, e.g., κ_r = 5 for M_s = 5 in Fig. 10. Then the RFI source detection also becomes conservative with decreasing false alarm rate. When κ_r is small, for example κ_r = 0.5 for M_s = 35, MUSIC spectrum deteriorate as shown in Fig. 10(f). The proposed rank estimation method gives M_s = 15 with κ_r = 1, and the case of M_s = 23 is obtained with κ_r = 0.9. As shown in Fig. 10 the proposed algorithm estimates the rank of covariance matrix around the elbow point of eigenvalue plot, and it produces appropriate results of MUSIC spectra.

REFERENCES

[1] Y. H. Kerr, P. Waldteufel, J. P. Wigneron, S. Delwart, F. Cabot, J. Boutin, M. J. Escorihuela, J. Font, N. Reul, C. Gruhier, S. E. Juglea, M. R. Drinkwater, A. Hahne, M. Martin-Neira, and S. Mecklenburg, "The SMOS Mission: New Tool for Monitoring Key Elements ofthe Global Water Cycle," *Proc. IEEE*, vol. 98, no. 5, pp. 666–687, 2010.

[2] J. Font, A. Camps, A. Borges, M. Martin-Neira, J. Boutin, N. Reul, Y. H. Kerr, A. Hahne, and S. Mecklenburg, "SMOS: The Challenging Sea Surface Salinity Measurement From Space," *Proc. IEEE*, vol. 98, no. 5, pp. 649–665, 2010.

[3] K. McMullan, M. Brown, M. Martin-Neira, W. Rits, S. Ekholm, J. Marti, and J. Lemanczyk, "SMOS: The Payload," *IEEE Trans. Geosci. Remote Sens.*, vol. 46, no. 3, pp. 594–605, Mar. 2008.

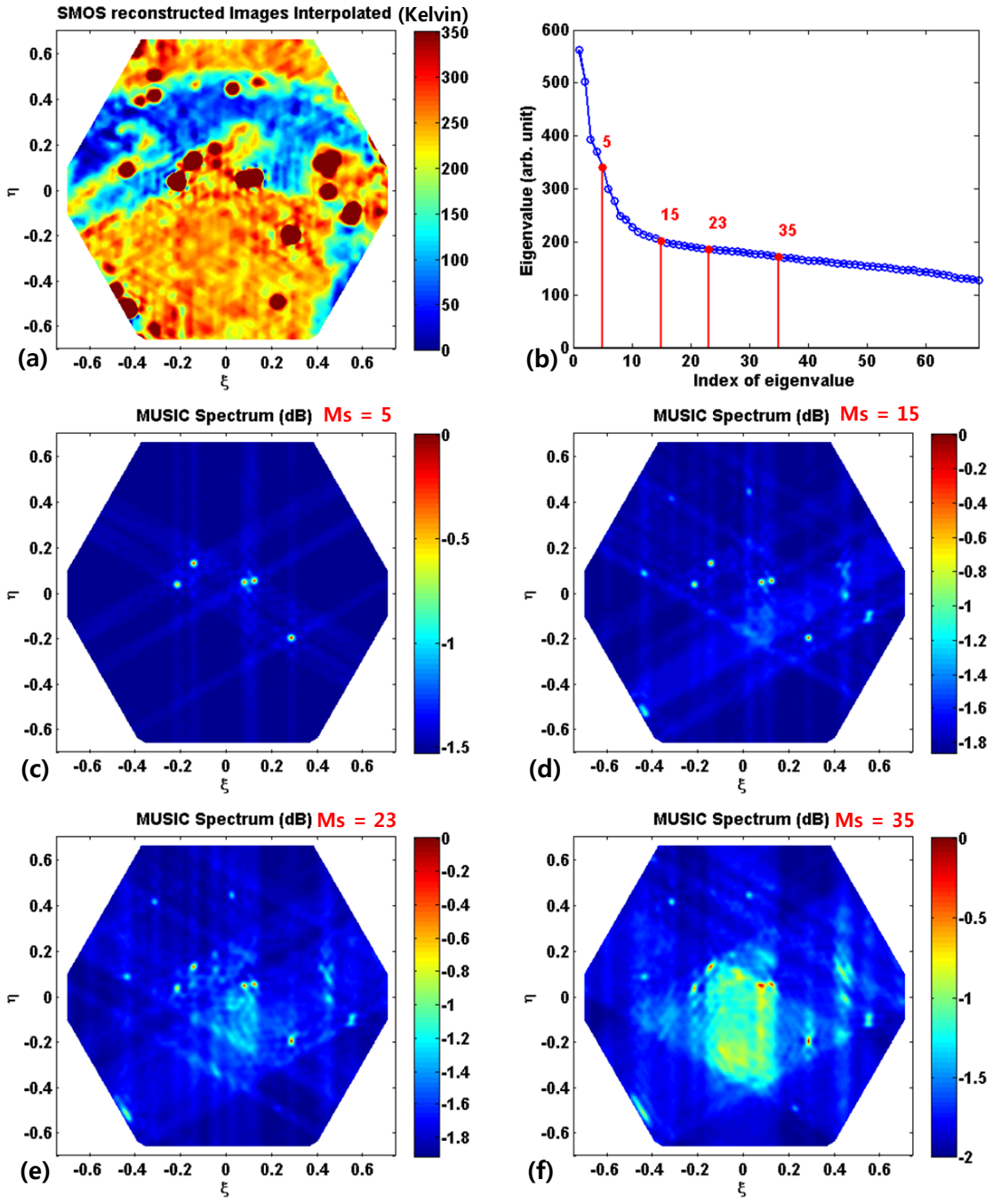

Fig. 10. Comparison of the MUSIC spectra estimated with different rank: (a) DFT result, (b) eigenvalue plot. MUSIC spectra with the rank of (c) M_s = 5, (d) M_s =15, (e) M_s = 23, and (f) M_s = 35.

[4] ITU, "ITU-R Radio Regulations footnote 5.340, Int. Telecommun. Union, Ra- dio Regulations 2012. Vol. I, Chapter II, Article 5 (RR5-64)." 2012. [Online]. Available: http://www.itu.int/pub/R-REG-RR/en

[5] R. Oliva, E. Daganzo, Y. H. H. Kerr, S. Mecklenburg, S. Nieto, P. Richaume, and C. Gruhier, "SMOS Radio Frequency Interference Scenario: Status and Actions Taken to Improve the RFI Environment in the 1400-1427-MHz Passive Band," *IEEE Trans. Geosci. Remote Sens.*, vol. 50, no. 5, pp. 1427–1439, 2012.

[6] M. Aksoy and J. T. Johnson, "A Study of SMOS RFI Over North America," *Geosci. Remote Sens. Lett. IEEE*, vol. 10, no. 3, pp. 515–519, May 2013.

[7] E. Daganzo-Eusebio, R. Oliva, Y. H. Kerr, S. Nieto, P. Richaume, and S. M. Mecklenburg, "SMOS Radiometer in the 1400 -1427-MHz Passive Band: Impact of the RFI Environment and Approach to Its Mitigation and Cancellation," *IEEE Trans. Geosci. Remote Sens.*, vol. 51, no. 10, pp. 4999–5007, 2013.

[8] A. Camps, J. Gourrion, J. M. Tarongi, M. Vall Llossera, A. Gutierrez, J. Barbosa, and R. Castro, "Radio-Frequency Interference Detection and Mitigation Algorithms for Synthetic Aperture Radiometers," *Algorithms*, vol. 4, no. 4, pp. 155–182, Aug. 2011.

[9] A. Camps, J. Gourrion, J. M. Tarongi, A. Gutie?rrez, J. Barbosa, R. Castro, and A. Gutierrez, "RFI analysis in SMOS imagery," in *Geosci. Remote Sens. Symp. (IGARSS), 2010 IEEE Int.*, 2010, pp. 2007–2010.

[10] R. Castro, A. Gutiérrez, and J. Barbosa, "A First Set of Techniques to Detect Radio Frequency Interferences and Mitigate Their Impact on SMOS Data," *Geosci. Remote Sensing, IEEE Trans.*, vol. 50, no. 5, pp. 1440–1447, 2012.

[11] A. Camps, H. Park, and V. Gonzalez-Gambau, "An imaging algorithm for synthetic aperture interferometric radiometers with built-in RFI mitigation," in *2014 13th Spec. Meet. Microw. Radiom. Remote Sens. Environ. IEEE*, Mar. 2014, pp. 39–43.

[12] Y. Soldo, A. Khazaal, F. F. Cabot, P. Richaume, E. Anterrieu, and Y. H. Kerr, "Mitigation of RFIs for SMOS: A distributed approach," *IEEE Trans. Geosci. Remote Sens.*, vol. 52, no. 11, pp. 7470–7479, Nov. 2014.

[13] H. Park, A. Camps, and V. Gonzalez-Gambau, "Accurate geolocation of RFI sources in SMOS imagery based on superresolution algorithms," in *2014 13th Spec. Meet. Microw. Radiom. Remote Sens. Environ. IEEE*, Mar. 2014, pp. 29–32.

[14] H. Park, V. González-Gambau, and A. Camps, "High Angular Resolution RFI Localization in Synthetic Aperture Interferometric Radiometers Using Direction-of-Arrival Estimation," *IEEE Geosci. Remote Sens. Lett.*, vol. 12, no. 1, pp. 102–106, 2015.

[15] R. Oliva, S. Nieto, and F. Felix-Redondo, "RFI Detection Algorithm: Accurate Geolocation of the Interfering Sources in SMOS Images," *Geosci. Remote Sensing, IEEE Trans.*, vol. 51, no. 10, pp. 4993–4998, 2013.

[16] Y. Soldo, F. Cabot, A. Khazaal, M. Miernecki, E. Slominska, R. Fieuzal, and Y. H. Kerr, "Localization of RFI Sources for the SMOS Mission: A Means for Assessing SMOS Pointing Performances," in *IEEE J. Sel. Top. Appl. Earth Obs. Remote Sens.*, vol. 8, no. 2, pp. 617627, 2015.

[17] S. Misra and C. S. Ruf, "Analysis of Radio Frequency Interference Detection Algorithms in the Angular Domain for SMOS," *IEEE Trans. Geosci. Remote Sens.*, vol. 50, no. 5, pp. 1448–1457, May 2012.

[18] E. Anterrieu, "On the Detection and Quantification of RFI in L1a Signals Provided by SMOS," *IEEE Trans. Geosci. Remote Sens.*, vol. 49, no. 10, pp. 3986–3992, 2011.

[19] A. Khazaal, F. Cabot, E. Anterrieu, and Y. Soldo, "A kurtosis-based approach to detect RFI in SMOS image reconstruction data processor," *IEEE Trans. Geosci. Remote Sens.*, vol. 52, no. 11, pp. 7038–7047, Nov. 2014.

[20] I. Corbella, F. Torres, N. Duffo, V. Gonzalez, A. Camps, and M. Vall-llossera, "Fast Processing Tool for SMOS Data," in *2008 IEEE Int. Geosci. Remote Sens. Symp. - IGARSS*, Jul. 2008, vol. 2., pp. II-1152–II-1155.

[21] H. Park, J. Choi, V. Katkovnik, and Y. Kim, "Interferometric Microwave Radiometers for High-Resolution Imaging of the Atmosphere Brightness Temperature Based on the Adaptive Capon Signal Processing Algorithm," *Environ. Monit. Assess.*, vol. 92, no. 1-3, pp. 59–72, 2004.

[22] P. Stoica and R. L. Moses, *Spectral analysis of signals*. Pearson/Prentice Hall Upper Saddle River, NJ, 2005.

[23] H. Trees, *Detection, Estimation, and Modulation Theory, Optimum Array Processing*. John Wiley & Sons, 2002.

[24] M. Wax and T. Kailath, "Detection of signals by information theoretic criteria," *IEEE Trans. Acoust.*, vol. 33, no. 2, pp. 387–392, Apr. 1985.

[25] M. Wax, "Detection and localization of multiple sources via the stochastic signals model," *IEEE Trans. Signal Process.*, vol. 39, no. 11, pp. 2450–2456, 1991.

[26] P. Djuric, "A model selection rule for sinusoids in white Gaussian noise," *IEEE Trans. Signal Process.*, vol. 44, no. 7, pp. 1744–1751, Jul. 1996.

[27] A. Camps, J. Bara, I. C. Sanahuja, and F. Torres, "The processing of hexagonally sampled signals with standard rectangular techniques: application to 2-D large aperture synthesis interferometric radiometers," *Geosci. Remote Sensing, IEEE Trans.*, vol. 35, no. 1, pp. 183–190, 1997.

[28] J. Serra, *Image analysis and mathematical morphology, v.1*. Academic Press, 1982.

[29] F. Y. Shih, *Image processing and mathematical morphology: fundamentals and applications*. CRC Press, 2009.

[30] F. Cabot, Y. H. Kerr, and P. Waldteufel, "Calibration of SMOS geolocation biases," in *2007 IEEE Int. Geosci. Remote Sens. Symp.* IEEE, 2007, pp. 4448–4450.